A portable blood plasma clot micro-elastometry device based on resonant acoustic spectroscopy

C. R. Krebs,[1,a)] Ling Li (李灵),[2,a)] Alisa S. Wolberg,[3] and Amy L. Oldenburg[1,2,b)]

[1]*Department of Biomedical Engineering, University of North Carolina at Chapel Hill, Chapel Hill, North Carolina 27599, USA*
[2]*Department of Physics and Astronomy, University of North Carolina at Chapel Hill, Chapel Hill, North Carolina 27599, USA*
[3]*Department of Pathology and Laboratory Medicine, University of North Carolina at Chapel Hill, Chapel Hill, North Carolina 27599, USA*

Abnormal blood clot stiffness is an important indicator of coagulation disorders arising from a variety of cardiovascular diseases and drug treatments. Here, we present a portable instrument for elastometry of microliter volume blood samples based upon the principle of resonant acoustic spectroscopy, where a sample of well-defined dimensions exhibits a fundamental longitudinal resonance mode proportional to the square root of the Young's modulus. In contrast to commercial thromboelastography, the resonant acoustic method offers improved repeatability and accuracy due to the high signal-to-noise ratio of the resonant vibration. We review the measurement principles and the design of a magnetically actuated microbead force transducer applying between 23 pN and 6.7 nN, providing a wide dynamic range of elastic moduli (3 Pa–27 kPa) appropriate for measurement of clot elastic modulus (CEM). An automated and portable device, the CEMport, is introduced and implemented using a 2 nm resolution displacement sensor with demonstrated accuracy and precision of 3% and 2%, respectively, of CEM in biogels. Importantly, the small strains (<0.13%) and low strain rates (<1/s) employed by the CEMport maintain a linear stress-to-strain relationship which provides a perturbative measurement of the Young's modulus. Measurements of blood plasma CEM versus heparin concentration show that CEMport is sensitive to heparin levels below 0.050 U/ml, which suggests future applications in sensing heparin levels of post-surgical cardiopulmonary bypass patients. The portability, high accuracy, and high precision of this device enable new clinical and animal studies for associating CEM with blood coagulation disorders, potentially leading to improved diagnostics and therapeutic monitoring. © 2015 AIP Publishing LLC. [http://dx.doi.org/10.1063/1.4926543]

I. INTRODUCTION

A. Motivation

Abnormal structure and mechanical properties of blood clots are associated with cardiovascular disorders such as coronary artery disease (CAD),[1] myocardial infarction (MI),[2] diabetes,[3,4] and multiple myeloma.[5] In particular, clot stiffness, i.e., clot elastic modulus (CEM), has recently emerged as a tool for understanding hemostasis and classifying a variety of cardiovascular diseases (CVDs) and coagulopathies. CEM is dictated by the mechanical properties and available quantity of its constituent proteins and blood cells such as fibrin, platelets, and erythrocytes in a given pathological state. Interestingly, abnormal fibrin fiber thickness, density, and resistance to clot degradation (fibrinolysis) have each been associated with thromboembolic diseases and bleeding disorders.[6–8] Similarly, abnormal fibrinolysis and reduced clot strength have also been shown to be significant indicators of mortality rates in severe trauma.[9] Thus, CEM provides direct insight into blood clot structure, which offers the potential to impact both our understanding of coagulation disorders and the surgical management of hemostasis. This work presents a portable micro-elastometry device for highly accurate measurements of CEM. The use of microliter blood volumes enables its application toward research using small animal models, while the compact size and portability of the instrument have the potential to enable new translational studies in a clinical setting.

From a clinical perspective, the immediate importance of such a device rests in its ability to provide accurate and repeatable diagnostic information about clot structure and clot formation during surgery. In 2010, there was one death every 40 s in the USA as a result of CVD,[10] and many of these patients required surgical intervention. At present, cardiopulmonary bypass and heart transplant surgeries employ the use of dose dependent heparin anticoagulation to avoid thromboembolic events secondary to clot formation. Maintaining an appropriate level of anticoagulation during surgery while reversing the effects of heparin after surgery is critical for reducing patient complications such as postoperative bleeding. Heparin management, however, is still largely determined by activated coagulation time (ACT), a method with poor sensitivity and lack of correlation with heparin post-surgical rebound, while physical measures using thromboelastography

---

(TEG) have indicated higher sensitivity.[11–13] To illustrate the clinical significance of CEM and its potential relevance in managing surgical hemostasis, here we demonstrate the sensitivity of our device to varying plasma levels of heparin.

B. Clot elastometry

Blood clots offer particular challenges to mechanical analysis. For example, biological factors such as platelet activity and coagulation rate induce time-dependent changes, while factors within a mechanical measurement apparatus, such as strain amplitude and strain rate, can induce variability in the resulting measurements. Measuring the CEM (Young's modulus) fundamentally requires instrument sensitivity to longitudinal stress (force) and strain (displacement). In contrast to mechanical analyzers used for structural materials, the inherent softness (CEM <5 kPa) of blood and plasma requires an instrument with particularly delicate force and displacement sensitivity. At the same time, microliter sample volumes afford researchers the ability to perform fewer replicate sample blood collections and parallel analysis with remaining sample volumes more amenable to animal research. One of the most prevalent commercial clot mechanical analyzers is the TEG, which provides measurements of the clot reaction time, rate of clot formation, and clot strength. However, to date, TEG lacks standardization and has limited repeatability and diagnostic sensitivity.[14] TEG and related instruments, such as ROTEM and Hemodyne, are types of shear rheometers, where a cup containing the sample is moved relative to a pin or cone inserted into the sample to measure shear stress under controlled shear strain.[5,15] Research-based shear rheometers are also commonly used for characterizing CEM as a function of both strain amplitude and frequency.[16,17] Typically, these types of measurements employ relatively large strain in order to produce adequate stress for detection, which can induce non-linearity in the stress-strain response; blood clots, in particular, are known to be strain-stiffening.[18]

To improve the force sensitivity, cantilevers are often used, such as in atomic force microscopy (AFM). While AFM has found utility in describing the mechanical properties of individual fibrin fibers,[19] the ability to measure the bulk clot properties requires a larger surface area of contact, a non-ideal condition on a standard AFM instrument. Recently, a cantilever was developed specifically for soft material analysis and validated in biogels,[20] although it remains to be demonstrated in materials with elastic moduli <1 kPa, such as that of blood plasma. Another promising strategy is the use of a torsion pendulum with which the free oscillations are recorded in response to release of a shear stress,[21] a method employed with success for characterizing the viscoelasticity of blood clots.[1] The torsion pendulum shares some similarities with the technique described in this paper, resonant acoustic spectroscopy with optical vibrometry (RASOV), as will be discussed below.

C. Clot micro-elastometry using RASOV

The use of a system resonance to provide a strong signal-to-noise ratio (SNR) for measurement is a long-utilized technique for the development of instruments. In the field of elastometry, the shift in resonance of a high-Q cantilever has been shown as an accurate method for measuring thin films in the gigaPascal range.[22] Similarly, shifts in the frequency of a quartz crystal have been used to study coagulation by semi-quantification of the viscoelastic mass.[23] Instead of using a separate resonating material, in the technique called resonant ultrasound spectroscopy (RUS), one measures the mechanical resonance spectrum of the sample directly, and knowing the sample geometry, the components of the elastic tensor can be inferred.[24] While RUS is employed to characterize stiff materials, it was found that soft biogels and tissues exhibit resonances with sufficiently high Q (~3) to enable mechanical analysis.[25] For simplicity, one assumes the tissue is mechanically isotropic in order to extract a single value of elastic modulus from the observed fundamental longitudinal mode. These resonances typically occur in the acoustic (Hz-kHz) range due to the softness of the materials. Recently, some of the co-authors developed this method into a blood elastometer where a blood sample is allowed to clot in a microwell, and a microbead transducer placed atop the sample is subsequently frequency-swept, while an optical system was used to detect the microbead; this was dubbed RASOV.[26] RASOV was shown to provide improved repeatability relative to TEG when analyzing whole blood samples; the improvements are attributed to the use of acoustic resonances, a fixed geometry microwell with closed-boundaries, low actuator inertia, and minimal actuation forces.[27] Interestingly, using the resonance frequency to infer elastic modulus is physically the same as using the free oscillation frequency via the torsion pendulum; however, the SNR of the resonance measurement is able to be arbitrarily improved by using a slower frequency sweep, whereas the free oscillation signal is limited in SNR by the damping rate which shortens the available measurement time window.

In this paper, we report the construction of a RASOV system tailored for CEM measurement that is compact, portable, and automated, called "CEMport," to enable future clinical studies. Importantly, this instrument offers improved displacement resolution via a compact commercial displacement sensor to increase the dynamic range. As will be shown, this has allowed us to fully characterize the range of strains in the CEMport that provides accurate measurements of CEM within the linear viscoelastic regime. Below, we begin by reviewing the measurement principles of RASOV and lay out the quantitative design metrics that are used to optimally design CEMport for analysis of blood and plasma samples. After calibration and characterization of the device performance, we perform a study in human plasma samples spiked with heparin to investigate the potential application of the CEMport for aiding in heparin management.

II. METHODS

A. Measurement principle

In this section, we discuss the physical model and method of RASOV for elasticity measurement. RASOV measures the linear, isotropic elastic modulus of soft biological gels and

clots of controlled size by preparing them within a microwell. The linearity of the elasticity measurement is ensured by inducing a small uniaxial strain to the specimen; evidence that the strain is sufficiently small will be presented in Section III. Under this operational condition, the sample can be viewed as a linear-shift-invariant (LSI) system. The concept of the impulse response of a LSI system is then used to extract mechanical properties of the specimen.[28] Following linear elastic theory,[29] the elastic modulus of an elastically isotropic specimen of known size and boundary conditions can be expressed in terms of the fundamental resonant frequency of the longitudinal vibration,[25,26]

$$E = a_0 \rho f_0^2, \tag{1}$$

where E is the CEM, ρ is sample mass density, f_0 is the fundamental resonant frequency, and a_0 is an experimentally determined calibration coefficient that depends on the specimen's geometry, boundary conditions, and Poisson's ratio.

In order to measure f_0, RASOV involves applying a chirped (frequency-swept), sinusoidal driving force to the sample, $F(t)$, and the system impulse response is inferred from the measured displacement, Δz. First, let us consider the steady-state solution for a driving force at fixed frequency, ω. The resultant displacement can be modeled assuming linear viscous damping and elasticity according to the driven, damped, harmonic oscillator model,[30]

$$\Delta z''(t) + \gamma_0 \Delta z'(t) + \omega_0^2 \Delta z(t) = q \propto F(t), \tag{2}$$

where q is proportional to the driving force, ω is the angular frequency of the driving force waveform, and γ_0 and $\omega_0 = 2\pi f_0$ are the damping coefficient and natural angular frequency for the fundamental vibration mode, respectively, where f_0 is the corresponding natural frequency. For a complex driving force waveform, $\tilde{F}(t) = F(t)e^{i\omega t}$, the complex displacement solution can be written as

$$\Delta \tilde{z}(t) = \tilde{A}(\omega)e^{i\omega t}, \tag{3}$$

where the amplitude is described by a complex Lorentzian function

$$\tilde{A}(\omega) = \frac{q}{\omega_0^2 - \omega^2 + i\omega\gamma_0}. \tag{4}$$

In a RASOV measurement where $\tilde{F}(t)$ is a chirped sinusoidal waveform, the mechanical system response, $\tilde{I}(\omega)$, is characterized by the frequency-domain transfer function of the LSI system as follows:

$$\tilde{I}(\omega) = \frac{\Phi[\Delta z(t)]}{\Phi[F(t)]} \propto \tilde{A}(\omega), \tag{5}$$

where Φ is the Fourier transform operator. The magnitude of $\tilde{I}(\omega)$ represents the magnitude of the vibration, while the argument represents the phase difference between the vibration waveform (strain) and the driving force waveform (stress). Importantly, the Lorentzian solution predicts a phase transition from 0 to π across the fundamental resonance mode, which indicates a transition from stress and strain being in-phase to being exactly opposed.[25] An example of this phenomenon from a RASOV measurement of a plasma sample is shown in Fig. 1. The fundamental natural frequency f_0 is thus obtained
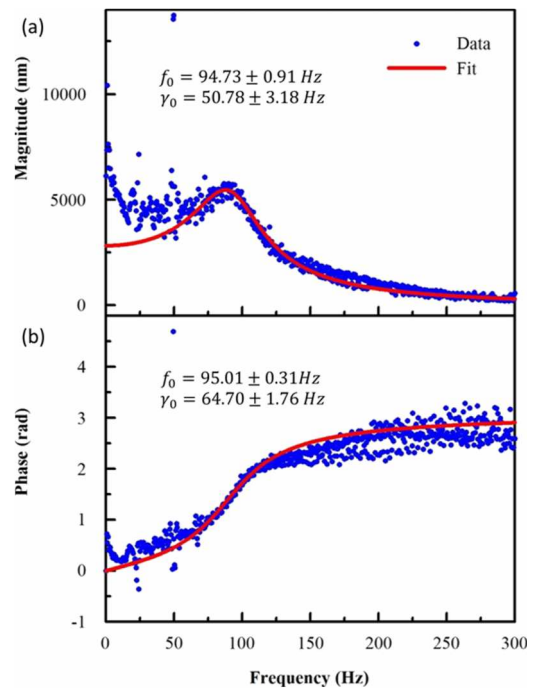

FIG. 1. Example data set showing the (a) magnitude and (b) phase of $\tilde{I}(\omega)$ obtained from a RASOV measurement of normal platelet-poor plasma (NPP).

by fitting the magnitude and/or phase of $\tilde{I}(\omega)$ to the Lorentzian solution, Eq. (4), and the corresponding CEM is then derived using Eq. (1). The data processing procedure is deferred to Subsection II F. Importantly, this measurement of CEM represents the storage modulus at the strain rate dictated by the resonance frequency; RASOV does not provide frequency-dependent elastic properties. As discussed below, we do not expect CEM to be significantly frequency-dependent in the regime of strain rates applied by RASOV but rather to represent the low strain rate (perturbative) value.

B. The microbead transducer

In the CEMport, the driving force is provided by magnetically actuating a steel microbead transducer on top of the specimen via a solenoid electromagnet positioned underneath the specimen (Fig. 2). An important factor when choosing a microbead transducer is its inertial mass. It has been shown that heavier transducers will lower the observed resonant frequencies.[31] In the other extreme, magnetic nanoparticles can be embedded into the sample for transduction;[25] however, these have been found to interfere with clotting processes for CEM measurement. In the CEMport, a chrome steel microbead of 0.7 mg and 500 μm diameter (grade 25, Salem ball company) is chosen as the transducer by merit that it is large enough to handle with tweezers and to provide sufficiently large magnetic gradient force but light enough to limit its perturbation to the resonance of the specimen. Within an externally applied magnetic field, the intensity and direction of the transduction force are determined by the magnetic properties of the microbead and shape of the local magnetic field lines, respectively. The microbead is pulled in $\hat{z}$ (vertically) by the electromagnet via the coupling between its induced magnetic dipole moment,
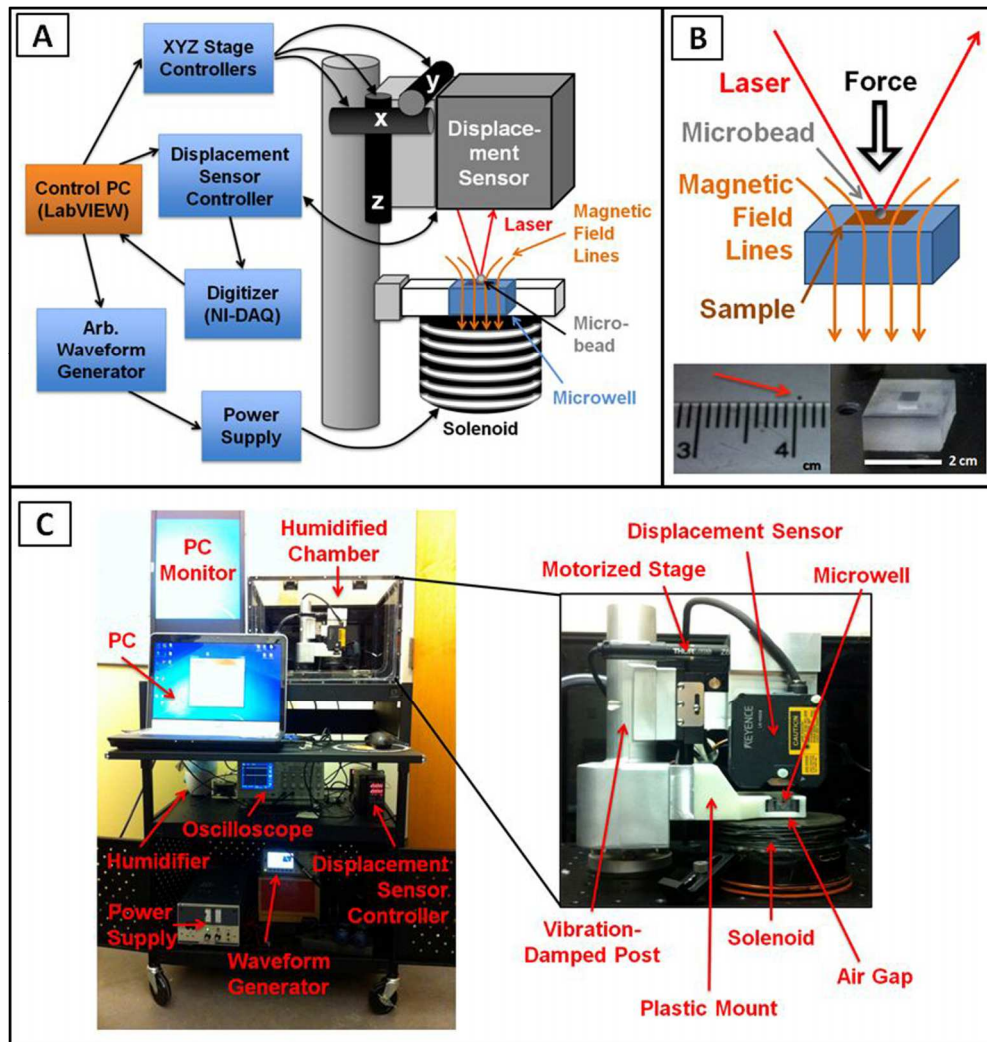
FIG. 2. (a) Schematic of the signal and device components of the CEMport. (b) An enlarged view schematic of the sample microwell. Insets display photographs of the 500 μm bead (small red arrow) and the sample microwell. (c) Photographs of the CEMport with major components indicated. Left: overall view of the portable cart. Right: layout within the humidified chamber. Blood clots prepared within the plastic microwell are slid into a plastic mount; the use of plastic avoids induced currents during operation of the solenoid electromagnet. A small air gap and vibration-damped mounting post ensure that the microwell and displacement sensor are mechanically isolated from the solenoid during RASOV.

m, and the external magnetic field, B. The induced dipole moment is linear in B for small applied fields. The B field is proportional to the solenoid current, which is proportional to the driving voltage V at the frequencies used in this system where inductance is negligible. Thus, the force waveform is proportional to the square of the voltage driving the electromagnet,

$$F(t) = (m \cdot \nabla) B \propto (B \cdot \nabla) B \propto V(t)^2 \hat{z} \qquad (6)$$

where the coefficient of proportionality is dependent on the magnetic susceptibility and volume of microbead, its separation from the solenoid, and the properties of the solenoid (turn density and electrical resistance). The direction of the force is along the $\hat{z}$ axis when the mircobead is properly placed within the central axis of the solenoid winding; furthermore, the sample holder is aligned with the solenoid so that the resulting transduced force is applied normal to the specimen surface and at its center (Fig. 2(b)). This alignment is important to avoid possible shear strains in $\hat{x}$ and $\hat{y}$ that induce torsional

vibrational modes instead of the desired longitudinal modes, which complicate the resonant acoustic spectral analysis.

Importantly, the microbead transducer is designed to deliver a relevant range of forces for accurate measurement of CEM. Let us define the magnetic gradient force according to Eq. (6) as $(B \cdot \nabla) B$, which has units of T^2/m. The magnetic gradient force was measured via a Hall probe in the $\hat{z}$ direction at 2.0 cm above the surface of the coil and was found to range from $(6.0 \times 10^{-5}$–$1.78 \times 10^{-2})$ T^2/m over the $(0.25$–$10.0)$ Vpp range of the waveform generator. Estimating the volume magnetic susceptibility of the chrome steel microbead as 0.72 $\times 10^{-2}$ and using the known volume of the bead, the transduction force of the RASOV system is computed to be within the range of (22.5 pN–6.68 nN). Now, let us consider whether this range provides sufficient flexibility to accurately measure the CEM of blood samples. As shown in Section III, the optimal range of indentation amplitudes for accurate measurement in the RASOV system is (740 nm–7.5 μm) at resonance. This represents a dynamic amplitude, which can be related to a corresponding quasi-static indentation amplitude by dividing by

the quality factor, $Q = \omega_0/\gamma_0$, which is typically ≈ 15 for blood samples. Finally, we use the Hertz model of contact mechanics to relate the CEM, the quasi-static indentation amplitude, and the force applied by the microbead of known diameter.[32] If we consider the minimum CEM to be that obtained with the minimum available transduction force and maximum measurable indentation, and the maximum CEM to be that with the maximum force and minimum indentation, we obtain a dynamic range of the CEMport system of (3 Pa–27 kPa). This dynamic range is broad enough to cover the typical elasticity range of whole blood clots ($\sim$1.5 kPa–5 kPa),[26] plasma ($\sim$0.3 kPa–2 kPa),[33] and other materials with elastic moduli within this range.

C. Instrument design

The CEMport is a portable blood clot micro-elastometry instrument consisting of a laser displacement sensor, sample microwell, microbead transducer, solenoid electromagnet, motorized stages, sampling hardware, and LabVIEW-driven graphic user interface (GUI) (see Fig. 2). The solenoid is powered by a programmable 250 Watt power supply (KEPCO, Model ATE 36-8) which is modulated with a square-root sinusoidal, chirped voltage waveform (described in D below) via an arbitrary function generator (Agilent Technologies, Model 33522A). At present, the power supply is operated at 1/3rd of its capacity to reserve extra electrical power for the addition of two future solenoids. The solenoid coil consists of 18-American wire gauge (AWG), poly-thermaleze coated magnet wire (Allied Electronics) wrapped around a custom-machined Ultem (McMaster Carr) bobbin in $\sim$26 total layers and held in place with a thermally conductive and electrically insulating adhesive (Cast-Coat, Inc, CC3-301 AD). It was wound around the Ultem bobbin spindle with the following dimensions: 10 cm (outer diameter), 1.5 cm (height), and 1 cm (inner diameter). These dimensions were optimized via computational simulations to maximize the magnetic gradient force while achieving a compact prototype design ideal for portability. To avoid the need for water cooling, which would add unwanted bulk to the device, an automated triggering mechanism limits the electrical current through the coil to short-burst sampling intervals. To maintain a strong magnetic gradient force, a minimal gap between the solenoid and the microwell stage was maintained. At the same time, the magnet was mechanically decoupled from the stage to prevent vibrations induced within the magnet from directly shaking the microwell.

Displacement measurements were obtained with a commercial laser displacement sensor (Keyence, LK-H008) which delivers a 0.3 mW, 655 nm wavelength, and 20 μm spot size that is reflected from the surface of the bead. The laser is coupled to an associated controller (Keyence, LK-G5001) for triangulating the return trajectory of the beam via a RS-CMOS element. The displacement detection range and resolution were set to 20 μm and 2 nm, respectively, via the device software. Additionally, a low-pass, 1000 Hz filter setting was chosen on the controller to improve the signal-to-noise ratio at the lower frequencies relevant to the acoustic resonances in our experiments.

D. Instrument operation

In the CEMport, the procedure for RASOV measurement of a sample clotted within the microwell includes the steps of microbead placement, sample rate selection, peak-to-peak driving voltage selection, and maximum sweep frequency selection. Once these parameters are chosen by the user within the custom GUI (National Instruments, LabVIEW 2012), a series of discrete sampling scans occur to align the microbead with the displacement sensor laser prior to the acoustic scan.

The custom GUI was programmed to coordinate sample stage positioning, electromagnet waveform generation, displacement data acquisition, and subsequent data analysis. This offered a user-friendly interface for selecting the sampling rate (1–2 kS/s), waveform voltage amplitude (0.25–10.0 Vpp), and maximum sweep frequency (75–1000 Hz) prior to data acquisition. Immediately before a scan, the user sends a zeroing command to the displacement sensor to ensure the maximum available dynamic range of vibrations above and below the equilibrium position of the microbead. When initiating a scan, the GUI simultaneously signals the laser displacement sensor to collect data, signals the waveform generator to burst a pre-loaded waveform, and reads in the displacement data from a digitizer (National Instruments, USB-6009) connected to the displacement controller's analog output terminals.

Accurate data collection requires precise alignment of the microbead such that the laser reflects off the center of the bead. To automate this alignment process, the displacement sensor was mounted to a 3-axis motorized stage (Thor Labs, MT3-Z8) with associated controllers (Thor Labs, TDC001 T-Cube DC Servo) connected with the LabVIEW interface. The interface enables a 3D scan of the laser by rastering within a 1.5 mm $\times$ 1.5 mm x-y plane over 100 $\times$ 100 μm steps to locate the bead, incrementally dropping by 100 μm steps in z until bead recognition occurs. Scan times are typically 90 s after placement of a new sample, while successive measurements of the same sample only require a few seconds for realignment due to sample dehydration during data acquisition.

Finally, due to the high-water content of biosamples and the negative impact of sample dehydration on the assessment of CEM, a sealed, humidified chamber was constructed from acrylic panels and anodized structural beams (Makerbeam). The use of a humidified chamber provided a significant reduction in the sample dehydration rate, which was reduced from 245 nm/s to 81 nm/s for a 3 mg/ml agarose sample in the open air compared to an 85% humidified environment, respectively. Humidity control was accomplished through the use of a positive-feedback loop and a humidity sensor (AGPtek Digital Air Humidity Controller, model WH8040) wired to an electrical relay, which provided power to an off-the-shelf room humidifier (Holmes Ultrasonic Humidifier, model HM500TG) connected to the sealed chamber via rubber tubing.

E. Sample preparation and data collection

For RASOV, samples are prepared within fixed dimension microwells (5 mm (l) $\times$ 5 mm (w) $\times$ 6 mm (d)) corresponding

to a volume of 150 μL. The gelation microwell was 3-D printed from VeroBlue (RGD840), rigid, opaque photopolymer (Poly-Jet, Stratasys, Eden Prairie, MN). For instrument calibration and strain sensitivity measurements, agarose powder (Sigma-Aldrich #A0169, Type I-A, low EEO) was added to distilled water with varying concentrations (3–10 mg/ml) and was heated in a hot water bath (85 °C) for 20 min. Solutions were pipetted into microwells where they were allowed to cool at room temperature for at least 30 min within a sealed, humidified chamber. CEMport calibration data were then acquired within 210 min after preparation from 2 agarose samples at each concentration, collecting 10-30 consecutive measurements per sample. Additionally, 10 consecutive measurements per sample were collected for strain sensitivity data using a fresh agarose sample for each strain value to avoid ambiguity from sample dehydration.

Plasma samples of varying heparin concentrations were prepared in the CEMport microwells as follows. Pooled NPP was prepared from healthy human volunteers according to a protocol approved by the University of North Carolina Institutional Review Board, as described.[34] Stock heparin sodium (1 U/μL, APP Fresenius Kabi USA, LLC) was prepared at varying concentrations into buffer (150 mM NaCl and 96 mM benzyl alcohol). Samples were prepared by pipetting 10 μl calcium (150 mM stock solution), 10 μl diluted heparin or control buffer, and 25 μL tissue factor/lipids (Stago BNL, 6 pM/24 μM) into separate corners of the microwell; NPP (105 μL) was added as the final mixing step for the sample. This procedure resulted in final concentrations of 10 mM calcium, 0–0.27 U/ml heparin, and 1 pM/4 μM tissue factor/lipids. Samples were allowed to clot for 2-3 h before they were measured by RASOV. RASOV data were then acquired from 1 to 2 samples at each concentration, collecting 10-30 consecutive measurements per sample.

F. Signal processing

Here, we describe the signal processing steps used in the CEMport to convert the measured displacement signal into an estimate of f_0 according to Eqs. (4) and (5). We found that fitting data to the phase $\left(arg\left(\tilde{A}(\omega)\right)\right)$ was less error-prone than fitting data to the magnitude $\left(abs\left(\tilde{A}(\omega)\right)\right)$. For ultralow strain displacement signals, the phase shift from 0 to π at resonance is particularly distinct and is specific to induced modulations that are phase-locked to the transducer, rejecting randomly phased noise. To measure the acoustic resonance spectrum, the electromagnet voltage waveform was frequency-swept (chirped),

$$V(t) \propto \sqrt{\frac{1 - \cos\left(\pi k t^2\right)}{2}}, \tag{7}$$

where k is the linear chirp rate determined by the frequency sweep range (0–(300-1000)Hz) and the duration (2 s) of the scan. According to Eq. (6), the resulting force waveform is thus

$$F(t) \propto \frac{1 - \cos\left(\pi k t^2\right)}{2}. \tag{8}$$

This force waveform is used to calculate the frequency-domain transfer function, $\tilde{I}(\omega)$, according to Eq. (5), which is proportional to the complex specimen vibration, $\tilde{A}(\omega)$. The data

analysis script, an essential part of the instrument, employs Least Squares Fitting (LSF) to fit the amplitude and phase of $\tilde{A}(\omega)$ according to

$$\left|\tilde{A}(\omega)\right| \overset{LSF}{\to} \frac{q}{\sqrt{(\omega_0^2 - \omega^2)^2 + \gamma_0^2 \omega^2}}, \tag{9}$$

$$-Arg\left(\tilde{A}(\omega)\right) \overset{LSF}{\to} \tan^{-1}\frac{\gamma_0 \omega}{\omega_0^2 - \omega^2} + \beta\omega, \tag{10}$$

where q, ω_0, and γ_0 are free-fit parameters. The term $\beta\omega$ in Eq. (10) is added to account for imperfect synchronization between the waveform generator burst and the displacement sensor measurement. β represents the time lag between these events, which is up to ± 10 ms in our system. (A constant offset in time, after Fourier transformation, becomes a linear phase ramp in frequency.)

A semi-automated fitting routine was developed to provide an objective measurement of f_0 based upon RASOV data. The only input from the user is the frequency range over which to fit data, after which four steps are performed to robustly converge on the best-fit f_0. These steps are detailed in Table I. Amplitude data are first fitted to obtain a rough estimate of f_0 (step 1), while phase data in the frequency spectral range below the resonance are fitted to a straight line to obtain an estimate of the phase ramp, β (step 2). These two preliminary steps are used to pre-condition the phase data (by subtracting the phase ramp) and to provide initial guesses for a LSF of the phase data (step 3). Because of the relatively high dimensionality of the fitting (ω_0, γ_0, and β all being free-fit parameters), we found that an additional step is required to avoid a LSF convergence toward a possible local minimum. Thus, step 4 consists of incrementing the initial guess for β and obtaining the global minimum over all of the increments. Final phase fitting results are only retained when the corresponding coefficient of determination (R^2) is above 0.85.

III. RESULTS AND DISCUSSION

A. Strain sensitivity

Compared to the previous RASOV instrument,[26] the CEMport offers improved displacement sensitivity (from 6 nm to 2 nm) and improved maximum displacement (from 300 nm to 7510 nm) by switching from an optical imaging system (optical coherence tomography (OCT)) to a commercial displacement sensor (Keyence). Thus, CEMport effectively increases the available dynamic range of displacement from 50× to 3750×. These improvements have led to a larger window of transduction forces that provide an accurate measurement of CEM. Here, we characterize the strain dynamic range over which accurate measurements of CEM are obtained by the CEMport.

The dynamic range of peak-to-peak resonant displacement amplitudes over which the resonant frequency, f_0, is insensitive to the value of the strain is an important figure of merit of the CEMport. For strains that are too large, the sample is no longer linearly viscoelastic. For strains that are too small, the system noise is too great to obtain an accurate data fitting. Since the user will typically measure samples with unknown

TABLE I. Method for semi-automated fitting of RASOV data with the CEMport.

Step	Data	Data range (low ↔ high)	FFP[a]	→	IG[b]	→	(LB–UB)[c]	Model
1	Amplitude	User-defined[d]	ω_{01}	→	auto[e]	→	$(0 - f_{max})$[f]	Amplitude (Eq. (9))
			γ_{01}	→	auto	→	$(0 - 0.5 f_{max})$	
			p_{01}	→	auto	→	$(0 - 1.5 I_{peak})$[g]	
2	Phase (unwrapped)	$\frac{(\omega_{01} - \gamma_{01})}{2} \leftrightarrow (\omega_{01} - \gamma_{01})$	β_2	→	0	→	unbounded	$\phi_{ramp} = \beta_2 \omega$
3	Phase minus ϕ_{ramp}	$\frac{\omega_{01}}{5} \leftrightarrow f_{max}$	ω_{03}	→	ω_{01}	→	$(0 - f_{max})$	Phase (Eq. (10)), $\beta_{tot} = \beta_2 + \beta_3$
			γ_{03}	→	γ_{01}	→	$(0 - 0.5 f_{max})$	
			β_3	→	0	→	$(\pm 50 \text{ ms})$	
4	Phase minus $\beta_{tot}\omega$	$(\omega_{03} - \gamma_{03}) \leftrightarrow (\omega_{03} + \gamma_{03})$	ω_{04}	→	ω_{03}[h]	→	$(0 - f_{max})$	Phase (Eq. (10))
			γ_{04}	→	γ_{03}[h]	→	$(0 - 0.5 f_{max})$	
			β_4	→	incremented[i]	→	$(\pm 50 \text{ ms})$	

[a] *FFP*: free-fit parameter (ω: resonant frequency, γ: damping factor, and p: amplitude peak intensity).
[b] *IG*: initial guess for subsequent fitting.
[c] Lower (*LB*) and upper bound (*UB*) constraints for fitting parameters.
[d] The user initially defines a data range covering the fundamental resonance peak.
[e] The initial guesses for step 1 are determined automatically by peak-searching.
[f] f_{max} is the maximum frequency of the driving force waveform.
[g] I_{peak} is the maximum amplitude determined automatically by peak-searching.
[h] Final values of ω_{04} and γ_{04} are determined from the global minimum of multiple fits obtained while varying *IG* of β_4.
[i] *IG* of β_4 is incremented around a value of 0 to avoid local minima.

CEM and thus unknown peak amplitude, it is important to rapidly identify whether a given measurement is within this dynamic range. If needed, the driving voltage can be adjusted to achieve a measurement within this target.

Fig. 3(a) shows CEMport displacement data and associated amplitude and phase fittings with varying driving voltages to investigate the effect of strain. For this experiment, the samples consisted of agarose at a concentration of 3.36 mg/ml, which has an elastic modulus of 3.8 kPa. This is similar to the elastic modulus of whole blood clots, which exhibit CEM typically from 1.5 to 5 kPa.[26] Fig. 3(b) shows evidence that the fitted values of f_0 are within one standard deviation for strain amplitudes of 1.23×10^{-4} and 1.25×10^{-3} ($n = 10$ each), where the corresponding sample surface peak-to-peak displacements are 739 ± 24 nm and 7510 ± 730 nm, respectively. Two additional measurements obtained at 2.34×10^{-4} and 1.66×10^{-3} ($n = 2$ each) suggest that there is a plateau region over which f_0 is consistent within experimental error. At strains below and above this range, f_0 is significantly lowered from the ideal value and the semi-automated LSF routine is unable to obtain a sufficiently good fit for all 10 data scans. At the lowest strain measured, the low signal-to-noise ratio results in poor data fitting. At the highest strain measured, the data begin to deviate from the linear viscoelastic model, where the peak at approximately $1/2 f_0$ suggests nonlinearity in the mechanical response. Thus, we estimate that the dynamic range of the peak-to-peak strain amplitude in the CEMport is 1.23×10^{-4}–1.25×10^{-3}.

Given this result, it is important to address whether the maximum strain and strain rates employed by the CEMport are expected to lie within the linear viscoelastic regime of blood clots and the agarose calibration samples. The mechanical properties of blood clots are largely dictated by that of their fibrin network.[35] Mechanical measurements of fibrin both in bulk and on individual molecules show that a linear strain-stress relation holds for strains well above 1%,[17,36] which is significantly larger than the strain encountered during RASOV measurements. Frequency-dependent measurements of the shear modulus for fibrin clots suggest that the storage modulus is relatively constant for strain rates up to ~2/s.[17] In comparison, a typical blood clot of 4 kPa with resonance at 237 Hz would have a strain rate between 0.1/s and 1.0/s over the strain dynamic range of the CEMport. Thus, while smaller strains are more desirable to avoid potential nonlinearities, the CEMport is expected to provide consistent measurements of blood clots over its dynamic range of applied strains. Furthermore, the smaller resonant frequencies of plasma (as will be shown below) will have even lower strain rates and further relax this requirement. Similarly, it has been shown that agarose is highly linear for strains exceeding 1%,[37] while strain rates below ~3/s exhibit relatively constant shear moduli.[38] This observation suggests that for the maximum concentration agarose sample used in this study, with a resonance of ~600 Hz, it would be important to use a strain amplitude less than 8×10^{-4}, which is still well above the minimum peak-to-peak strain of 1.23×10^{-4}. Lower concentrations of agarose with lower resonant frequencies will relax this requirement. Overall, these results suggest that the perturbative nature of the CEMport is relevant for probing the small-strain, linear elastic moduli of blood and related biogels.

B. Device calibration

The value of the CEMport lies in its ability to profile acoustic resonances and to convert these values into calculated elastic modulus readings using Eq. (1). To calibrate the CEMport, we use agarose gel because it is easily prepared in both large and small sample sizes. The elastic modulus of
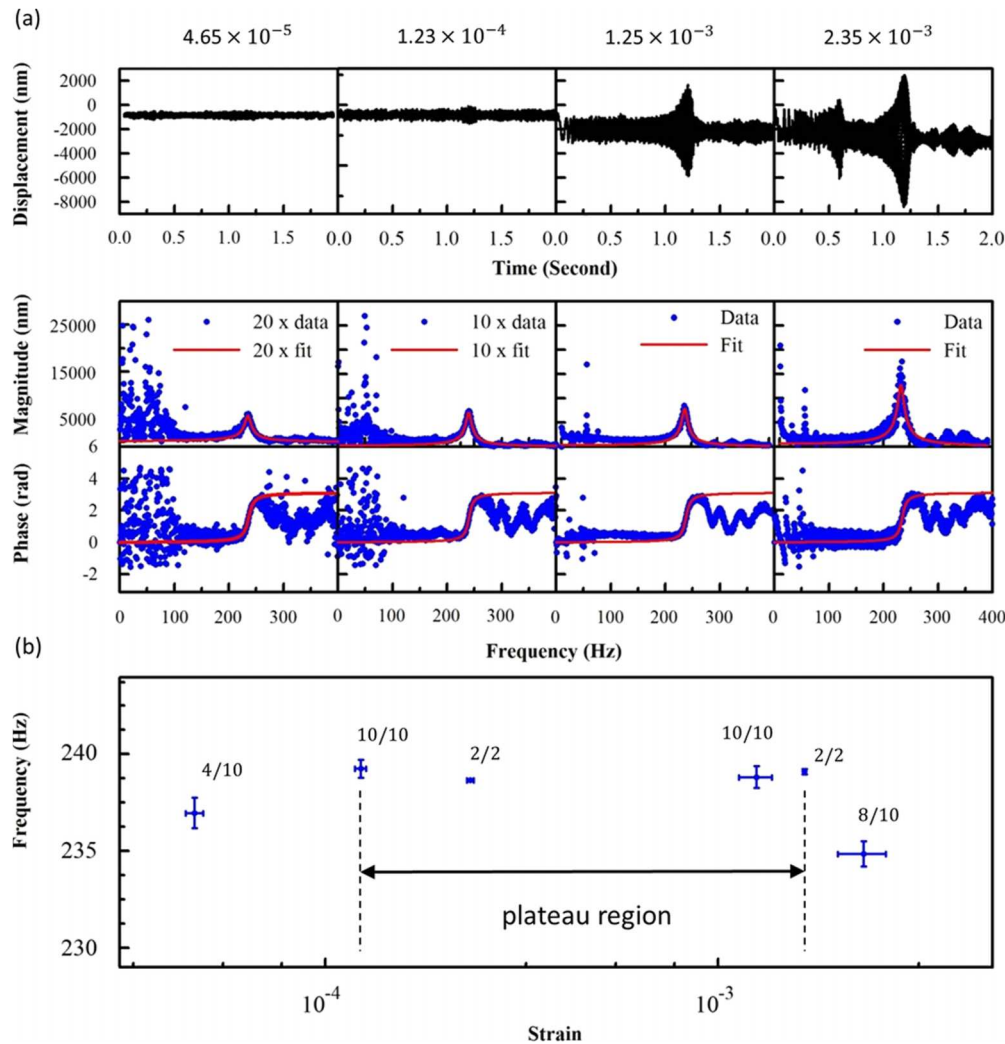
FIG. 3. CEMport measurements of agarose samples with varying maximum strain amplitudes by adjusting the solenoid voltage. (a) Top: raw displacement data versus time; bottom: corresponding amplitude and phase spectral data and their fitting to the Lorentzian model. (b) Fitted f_0 versus maximum strain amplitude. The number of successful fits is indicated for each data point (e.g., 4/10 means 4 out of 10), where only data with $R^2 > 0.85$ are considered successful.

agarose versus concentration can then be accurately measured via a commercial texture analyzer (using large samples) and related to RASOV measurements of resonant frequency over the same concentration range. Fig. 4 shows the calibration of the CEMport using agarose that has a known concentration-dependent elastic modulus according to texture analyzer data collected in our lab previously.[26] Similar to other reports, we have found that the concentration-dependent Young's modulus of agarose is consistent with a power-law of 2,[37] while we

have introduced an offset concentration, c_0, to represent the threshold value below which a gel does not form. The best-fit line reported in Fig. 4(a) is slightly different than that in Ref. 18 due to a different value of c_0 obtained from the RASOV data with which the texture analyzer data were subsequently fitted.

CEMport data collected across the same agarose concentration range suggest a linear relationship between concentration and resonant frequency (Fig. 4(b)). Combining the model fittings from the texture analyzer and the CEMport, the
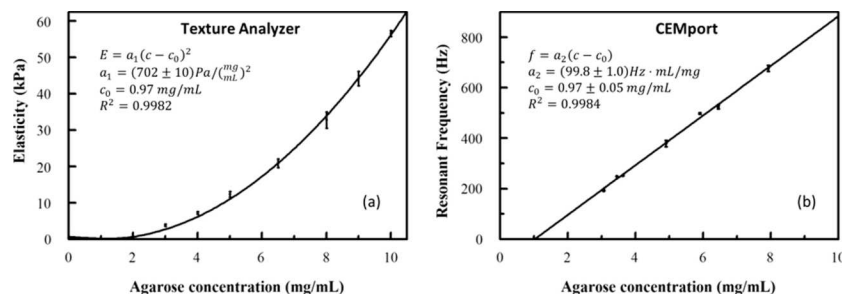

FIG. 4. Calibration of RASOV using agarose gels of varying concentrations. (a) Elastic moduli measured by a texture analyzer were fitted to a power-law function.[26] (b) Resonant frequencies measured by RASOV were fitted to a linear function. The functional description of RASOV's characteristic is obtained by combining the two modeling fittings (mean ± standard deviation).

resulting calibration between CEM and f_0 becomes

$$CEM = \left(\frac{a_1}{a_2^2}\right) f_0^2 = \left(0.071 \pm 0.002 \frac{\text{Pa}}{\text{Hz}^2}\right) \times f_0^2, \quad (11)$$

where a_1 and a_2 are coefficients from fitting elastic moduli obtained by the texture analyzer and resonant frequencies obtained by the CEMport, respectively. Importantly, this calibration constant is consistent with that from a previous study $(0.076 \pm 0.003 \text{ Pa/Hz}^2)$ in which a microwell of the same dimensions was used, but where RASOV was performed via an OCT system.[26] Compared to the CEMport described here, while OCT provided the ability to image the bead sitting on the sample, it is considerably more bulky, expensive, and not specifically designed for elastometry. The CEMport provides a portable and streamlined system for accurate and repeatable elastometry of blood samples.

In order to measure the CEM of an arbitrary sample, one must account for differences in the mass density of the sample, ρ, from that of the agarose used for calibration, according to Eq. (1). For example, when analyzing whole blood samples, this requires a small correction. Given that the density of agarose used to calibrate the CEMport is 1.0 g/ml, we thus compute the coefficient a_0 in Eq. (1) to be

$$a_0 = \frac{a_1}{a_2^2 \rho_{agarose}} = \left(0.071 \pm 0.002 \frac{\text{Pa} \cdot \text{ml}}{\text{Hz}^2 \cdot \text{g}}\right). \quad (12)$$

Using this value of a_0, then, one can use Eq. (1) with the known mass density of the sample and the measured f_0 to compute the CEM. The total CEM measurement uncertainty (accuracy) depends upon the error in a_0 and fitting error for f_0 for the data scan. In practice, we find that the fitting error for f_0 is typically ~0.2%, which is considerably smaller than that from the calibration constant, which is 2.8%.

C. Device precision

One of the advantages of RASOV over non-resonant methods such as TEG is the improved measurement precision. To investigate this precision, Fig. 5 shows a box-and-whisker plot of repeated measurements of two low-concentration agarose gels as samples with CEM similar to blood clots.

The repeated measurements of a 3.06 mg/ml agarose gel (17 consecutive measurements 2.66 ± 0.04 kPa) and a 3.62 mg/ml agarose gel (30 consecutive measurements 4.63 ± 0.04 kPa) suggested a precision on the order of 1%–2%. In comparison, our previous study showed that RASOV offered a measurement precision of ~5% in whole blood samples, compared to ~10% via TEG. While the precision when measuring whole blood may be expected to be higher than that of agarose, as we will show below, we find that accuracy is a greater concern than precision when measuring plasma samples. This finding illustrates that RASOV is capable of CEM measurements with high repeatability.

D. Heparin study

One potential application for CEMport is monitoring of the level of blood anticoagulants, which can aid in reducing post-operative complications. Heparin is a widely used anticoagulant that is intravenously administered before and during heart surgery. Here, we study the effect of heparin on CEM as measured by the CEMport. Fig. 6 illustrates the CEM of clots formed by NPP as a function of heparin concentration. There is a clear trend of decreasing CEM with increased heparin concentration, with a rapid transition between high (>500 Pa) and low (<350 Pa) CEM as the heparin concentration increased from 0.025 to 0.050 U/ml. At heparin concentrations above 1.8 U/ml, the samples were palpably less solid and the microbead transducer was more difficult to position. Above 4.0 U/ml, clots failed to form during the 2-3 h waiting period. This time-point was specifically chosen based on indications in the literature that both structural and viscoelastic steady-state will reach completion by approximately 2 h.[39,40]

Importantly, the values we previously measured for CEM in whole blood clots (~1.5–5.0 kPa)[26] and presently in NPP clots (552 ± 74 Pa) via RASOV are consistent with TEG measurements performed in whole blood (~1.5–5.0 kPa)[26] and plasma (423 ± 24 Pa as inferred from the reported data, recognizing that different sources of plasma may have different baseline CEM).[41] The significantly higher value of CEM for whole blood compared to NPP can be partially explained by the presence of red blood cells and platelets in the whole blood.[33] Moreover, there is a wide variation in blood components encountered in normal and pathological conditions such
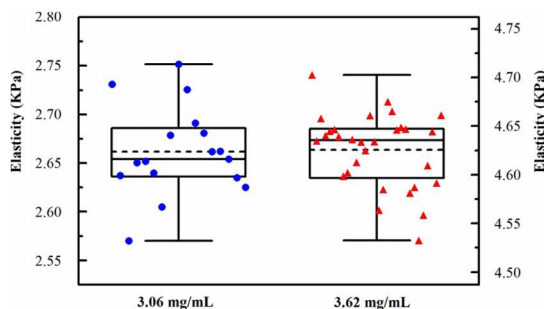

FIG. 5. Box-and-whisker plot of consecutive RASOV measurements of elasticity of a 3.06 mg/ml agarose gel (left with blue data circles) and a 3.62 mg/ml agarose gel (right with red data triangles). Measurement times were within a window of 18 min (left) and 12 min (right). The bottom, middle, and top solid lines of each box are defined by the first (25%), middle (50%), and third quartiles (75%) of corresponding data distribution. Horizontal dashed lines across the boxes are mean values of elasticity.
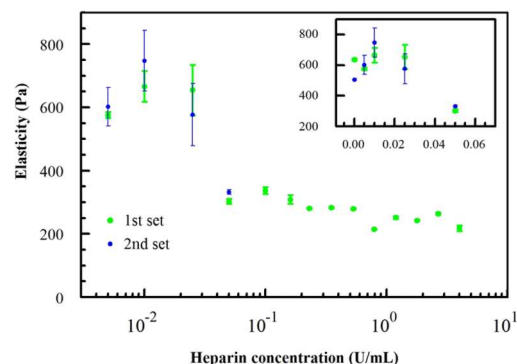

FIG. 6. CEMport measurements of normal platelet-poor plasma (NPP) versus heparin concentration. The inset displays a magnified view of low concentrations on a linear scale to include the zero concentration data point.

as thrombocytopenia and anemia. The literature suggests CEM ranges of 0.3 kPa–1.9 kPa and 2.3 kPa–4.4 kPa as a consequence of platelet and hematocrit variation, respectively.[33] These wide variations suggest the role of devices to more precisely profile platelet and red blood cell contributions to clot quality and consequently thrombotic disorders.

The precision (repeatability) for measurements obtained for individual control plasma samples was 1.2%. When averaging across 2 samples on 2 different days, the standard deviation increased to 12%. Thus, CEMport measurements of a single sample of NPP exhibit similar precision as that observed for agarose in Fig. 5. At the same time, the larger variability observed on different days suggests that there is some variability in the plasma itself, in the amount of time elapsed between preparing the clot and measurement (which was between 2 and 3 h), or in the mixing procedure to form a clot.

Importantly, the range of heparin concentrations employed here is physiologically relevant when compared with the circulating concentration of heparin observed in human patients after heparin administration. During cardiopulmonary bypass surgery, the concentration of heparin in whole blood was found to range from 2 to 4 U/ml,[42] which constitutes a highly anticoagulated state, consistent with our finding that NPP is difficult to clot above 1.8 U/ml and fails to clot above 4.0 U/ml. Heparin facilitates the antithrombin-mediated inactivation of thrombin which limits the conversion of fibrinogen to fibrin and alters the integrity of the fibrin fiber matrix during clot formation.[43] The mechanical properties of blood clots are strongly dictated by the fibrin matrix, in addition to red blood cells and platelets.[1,33,44] We previously found using RASOV that the CEM of purified fibrin clots increases as the square of the fibrinogen concentration. At the same time, reducing the thrombin concentration was associated with reduced CEM due to incomplete conversion of free fibrinogen into fibrin.[26] In whole blood, CEM was similarly reduced with increased concentration of low molecular weight heparin (as measured via antifactor Xa activity), while there was a positive correlation of antifactor Xa with thrombin generation time.[45] These previous observations are consistent with the observed trend in Fig. 6 of decreasing CEM with increasing heparin concentration, even at concentrations significantly below 1.8 U/ml where stable clots form.

Interestingly, the CEMport exhibited rapid CEM changes with heparin at exceedingly low concentrations of <0.05 U/ml, concentrations for which anticoagulation is not normally observed and measurements of heparin using antifactor Xa are difficult. This feature may be particularly relevant to post-surgical monitoring. Typically, protamine is administered after surgery to neutralize heparin and reverse the effects of anti coagulation. In this scenario, it has been found that plasma heparin concentrations can rise post-operatively to levels as high as 0.18 U/ml.[12] This heparin rebound effect poses possible risks of post-operative bleeding, which can increase morbidity and mortality.[46] The use of the CEMport may therefore aid in detecting low concentrations of heparin that reappear after protamine therapy in order to mitigate such risks. A patient-specific CEM baseline could be established before surgery and protamine dosage adjusted to re-establish the baseline post-surgically. While the study here focused on plasma, future studies in whole blood may translate to a simple protocol for blood sampling in this clinical scenario.

IV. CONCLUSION

We have introduced for the first time a portable microelastometry device, CEMport, specifically designed for blood clot analysis using RASOV. RASOV associates the elastic modulus to the intrinsic mechanical resonance of a sample clotted inside a fixed dimension microwell. RASOV provides a resonant signal with inherently high signal-to-noise in comparison to single frequency techniques or free-oscillation methods such as the torsion pendulum. In this paper, we have fully developed the measurement principles and motivated the design of the microbead transducer to accurately measure CEM over the typical range of blood and plasma samples. These design metrics can be used as a template to construct RASOV-based elastometers tailored for other application spaces, such as soft tissues, where conventional mechanical analyzers often lack the force sensitivity needed to accurately measure elasticity.

We have described the construction and performance of the CEMport, the first portable RASOV-based device. The CEMport offers a large improvement in displacement dynamic range by employing a commercial displacement sensor, which leads to a large range of resonant strain amplitudes over which accurate CEM is obtained. Other improvements include mitigating the effects of sample dehydration by employing a humidified chamber, semi-automating the RASOV data fitting, and providing a user-friendly interface to rapidly obtain the CEM value. We have calibrated the system via a commercial mechanical analyzer ($R^2 > 0.998$) and have demonstrated the system precision (repeatability) when measuring biogels (1%-2%) and plasma (1.2%). Importantly, the CEMport maintains low strain dynamics which affords insight into the perturbative, linear viscoelastic properties of clots. Some challenges remain to streamline the CEMport operation. Manual voltage adjustments to the transducer are sometimes required to adjust the unknown sample's resonant vibration amplitude within the CEMport dynamic range, and this process could be automated. The need for manual bead placement and to scan to locate the bead by the displacement sensor adds time to the otherwise 4 s measurement procedure. We acknowledge that the current 2-3 h waiting period allowed for clot formation may overestimate the time needed to achieve maximum clot density, and most certainly, this time frame limits the device in its present state to research-based applications. However, with the newly introduced portability, accuracy, and precision advancements presented here, future efforts focusing on optimizing clotting times significantly shorter than 2-3 h, as well as improvements to the bead scanning algorithm, will allow us to begin considering CEMport use within a clinical setting such as operating rooms for real-time CEM measurements during and after surgery.

While the focus of this study was to quantify the elastic modulus (i.e., storage modulus), we expect that the damping factor, γ_0, in Eq. (4) can similarly be related to the loss modulus using RASOV. Damping factor values were tabulated as part of the fitting routine in this study; however, we note

that additional effort with a validating technique is needed to determine the accuracy of the values obtained in this way. Our preliminary efforts suggest that γ_0 has a similar trend as f_0 as a function of heparin concentration, so it remains to be seen whether damping can provide significant new insight into clot mechanics.

The development of a reliable and accurate microelastometry device creates legitimate opportunities within the clinical space that can directly impact the decision-making capabilities of surgical care. Current CEM testing modalities are limited by poor standardization, low diagnostic sensitivity, and poor repeatability. Importantly, this study shows that the CEMport exhibits high sensitivity to small plasma levels of heparin which are normally difficult to measure. This provides promising evidence to suggest that the CEMport may be useful for discerning heparin rebound following protamine administration after cardiac surgery. Other potential applications for the CEMport include monitoring treatments for hemophilia to aid in drug dosing, differentiating clot quality in stored blood products,[47] potentially diagnosing cardiovascular diseases such as CAD before symptomatic onset,[1] and providing hemostasis therapy guidance in traumatic coagulopathies.[9]

ACKNOWLEDGMENTS

[1] J. Collet, Y. Allali, C. Lesty, M. Tanguy, J. Silvain, A. Ankri, B. Blanchet, R. Dumaine, J. Gianetti, and L. Payot, Arterioscler., Thromb., Vasc. Biol. **26**(11), 2567 (2006).
[2] K. Fatah, A. Silveira, P. Tornvall, F. Karpe, M. Blombäck, and A. Hamsten, Thromb. Haemost. **76**(4), 535 (1996).
[3] T. Lund, A. Svindland, M. Pepaj, A.-B. Jensen, J. P. Berg, B. Kilhovd, and K. F. Hanssen, Diabetes Vasc. Dis. Res. **8**(4), 284 (2011).
[4] R. Marchi-Cappelletti and N. Suárez-Nieto, Invest. Clin. **51**(3), 315 (2010).
[5] M. E. Carr, Jr., Cell Biochem. Biophys. **38**(1), 55 (2003).
[6] A. S. Wolberg, Blood Rev. **21**(3), 131 (2007).
[7] R. A. Ariens, J. Thromb. Haemostasis **11**(Suppl 1), 294 (2013).
[8] A. Undas and R. A. Ariens, Arterioscler., Thromb., Vasc. Biol. **31**(12), e88 (2011).
[9] H. Schochl, T. Frietsch, M. Pavelka, and C. Jambor, J. Trauma: Inj., Infect., Crit. Care **67**(1), 125 (2009).
[10] A. S. Go, D. Mozaffarian, V. L. Roger, E. J. Benjamin, J. D. Berry, M. J. Blaha, S. Dai, E. S. Ford, C. S. Fox, and S. Franco, Circulation **129**(3), e28 (2014).
[11] A. Vonk, D. Veerhoek, C. E. van den brom, L. J. van barneveld, and C. Boer, J. Cardiothorac. Vasc. Anesth. **28**(2), 235 (2014).
[12] J. Ichikawa, M. Kodaka, K. Nishiyama, Y. Hirasaki, M. Ozaki, and M. Komori, J. Cardiothorac. Vasc. Anesth. **28**(4), 1015 (2014).
[13] G. P. Gravlee, L. D. Case, K. C. Angert, A. T. Rogers, and G. S. Miller, Anesth. Analg. **67**(5), 469 (1988).
[14] C. W. Whitten and P. E. Greilich, Anesthesiology **92**(5), 1223 (2000).
[15] R. Luddington, Clin. Lab. Haematol. **27**(2), 81 (2005).
[16] J. M. Zuidema, C. J. Rivet, R. J. Gilbert, and F. A. Morrison, J. Biomed. Mater. Res., Part B **102**(5), 1063 (2013).
[17] K. M. Weigandt, D. C. Pozzo, and L. Porcar, Soft Matter **5**(21), 4321 (2009).
[18] C. Storm, J. J. Pastore, F. C. MacKintosh, T. C. Lubensky, and P. A. Janmey, Nature **435**(7039), 191 (2005).
[19] W. Liu, C. Carlisle, E. Sparks, and M. Guthold, J. Thromb. Haemostasis **8**(5), 1030 (2010).
[20] A. Markidou, W. Y. Shih, and W.-H. Shih, Rev. Sci. Instrum. **76**(6), 064302 (2005).
[21] P. A. Janmey, J. Biochem Biophys Methods **22**(1), 41 (1991).
[22] T. H. Metcalf and X. Liu, Rev. Sci. Instrum. **84**(7), 075001 (2013).
[23] R. S. Lakshmanan, V. Efremov, S. M. Cullen, and A. J. Killard, Sens. Actuators, B **192**, 23 (2014).
[24] A. Migliori and J. Maynard, Rev. Sci. Instrum **76**(12), 121301 (2005).
[25] A. L. Oldenburg and S. A. Boppart, Phys. Med. Biol. **55**(4), 1189 (2010).
[26] G. Wu, C. R. Krebs, F. C. Lin, A. S. Wolberg, and A. L. Oldenburg, Ann. Biomed. Eng. **41**(10), 2120 (2013).
[27] A. L. Oldenburg, G. Wu, D. Spivak, F. Tsui, A. S. Wolberg, and T. H. Fischer, IEEE J. Sel. Top. Quantum Electron. **18**(3), 1100 (2011).
[28] B. P. Lathi, *Linear Systems and Signals* (Oxford University Press, 2009).
[29] A. E. H. Love, *A Treatise on the Mathematical Theory of Elasticity* (Cambridge University Press, 2013).
[30] I. G. Main, *Vibrations and Waves in Physics* (Cambridge University Press, 1993).
[31] G. Wu, A. S. Wolberg, and A. L. Oldenburg, Proc. SPIE **8214**, 82140G (2012).
[32] K. L. Johnson and K. L. Johnson, *Contact Mechanics* (Cambridge University Press, 1987).
[33] M. Carr, Jr. and S. Carr, Blood Coagulation Fibrinolysis **6**(1), 79 (1995).
[34] K. R. Machlus, E. A. Colby, J. R. Wu, G. G. Koch, N. S. Key, and A. S. Wolberg, Thromb. Haemostasis **102**(5), 936 (2009).
[35] J. W. Weisel, Biophys. Chem. **112**(2), 267 (2004).
[36] M. R. Falvo, O. V. Gorkun, and S. T. Lord, Biophys. Chem. **152**(1), 15 (2010).
[37] M. Benkherourou, C. Rochas, P. Tracqui, L. Tranqui, and P. Gumery, J. Biomech. Eng. **121**(2), 184 (1999).
[38] F. Pervin and W. Chen, in *Mechanically Similar Gel Simulants for Brain Tissues: Proceedings of the SEM Annual Conference, Society for Experimental Mechanics, June 7-10, 2010* (Indianapolis, IN, 2010), Paper No. 118, pp. 9–13.
[39] M. Aleman, C. Gardiner, P. Harrison, and A. Wolberg, J. Thromb. Haemostasis **9**(11), 2251 (2011).
[40] N. Kurniawan, J. Grimbergen, J. Koopman, and G. Koenderink, J. Thromb. Haemostasis **12**(10), 1687 (2014).
[41] L. Bochsen, P. I. Johansson, A. T. Kristensen, G. Daugaard, and S. R. Ostrowski, Blood Coagulation Fibrinolysis **22**(3), 167 (2011).
[42] P. Raymond, M. Ray, S. Callen, and N. Marsh, Perfusion **18**(5), 269 (2003).
[43] J. Hirsh, T. E. Warkentin, S. G. Shaughnessy, S. S. Anand, J. L. Halperin, R. Raschke, C. Granger, E. M. Ohman, and J. E. Dalen, Chest J. **119**(1_suppl), 64S (2001).
[44] K. C. Gersh, C. Nagaswami, and J. W. Weisel, Thromb. Haemostasis **102**(6), 1169 (2009).
[45] D. Brophy, E. Martin, A. Best, T. Gehr, and M. E. Carr, J. Thromb. Haemostasis **2**(8), 1299 (2004).
[46] A. Galeone, C. Rotunno, P. Guida, B. Assunta, G. Rubino, L. D. L. T. Schinosa, and D. Paparella, J. Cardiothorac. Vasc. Anesth. **27**(5), 853 (2013).
[47] N. Tynngård, M. Trinks, and G. Berlin, Transfusion **54**(6), 1562 (2013).